Electrochimica Acta 507 (2024) 145172

Contents lists available at ScienceDirect

Electrochimica Acta

journal homepage: www.journals.elsevier.com/electrochimica-acta

An impedance spectroscopy study to unravel the effect of water on proton and oxygen transport in PEM fuel cells

Tatyana Reshetenko [a], Ying Sun [b,c], Thomas Kadyk [b,d], Michael Eikerling [b,c,d], Andrei Kulikovsky [b,*]

[a] Hawaii Natural Energy Institute University of Hawaii Honolulu, Hawaii 96822, USA
[b] Forschungszentrum Jülich GmbH Theory and Computation of Energy Materials (IET–3) Institute of Energy and Climate Research, D–52425 Jülich, Germany
[c] RWTH Aachen University, Chair of Theory and Computation of Energy Materials, Faculty of Georecources and Materials Engineering, D–52062 Aachen, Germany
[d] Jülich Aachen Research Alliance, JARA Energy, D–52425 Jülich, Germany

ARTICLE INFO

Keywords:
Liquid water saturation
Electrochemical impedance
Inductive loop
Modeling
PEM fuel cells

ABSTRACT

A recent physics-based model for liquid and gaseous water transport in the cathode catalyst layer (CCL) is incorporated into our 1d + 1d model for the PEM fuel cell impedance. The model includes parametric dependencies of the CCL oxygen diffusivity and proton conductivity on the liquid saturation. Fitting of the 1d + 1d model to experimental impedance spectra of a PEM fuel cell reveals two intriguing effects. Contrary to common belief, the liquid water saturation in the CCL is nearly independent of cell current density due to the growing liquid pressure gradient that drives liquid water removal from the CCL. Further, the "dry" oxygen diffusivity of the catalyst layer increases with cell current density. Apparently, at small current density, electrochemical conversion proceeds primarily in narrow pores, where the Knudsen oxygen diffusivity is low. With growing current density, larger and better connected pores with higher oxygen diffusivity dominate in the current conversion, leading to increase in effective oxygen diffusivity observed in impedance spectroscopy data.

1. Introduction

Since the arrival of polymer-based proton conductors in the 1960's, PEM fuel cells have been a subject of high expectations and extensive research as a pollution-free alternative to internal combustion engines. Nafion and its analogs conduct protons only in a hydrated state, with the proton conductivity growing roughly linearly with water content [1]. This renders water management a critical issue for the PEM fuel cell performance.

Liquid water is produced in the oxygen reduction reaction (ORR) that proceeds in the cathode catalyst layer (CCL). Qualitatively, the effect of liquid water on CCL operation is twofold: (i) water improves the proton conductivity in the CCL, and (ii) it worsens oxygen diffusion to the catalyst sites. Understanding water transport is thus a key for optimal CCL design.

Electrochemical impedance spectroscopy (EIS) is a powerful tool for in-situ studies of processes in the CCL [2]. Generally, impedance spectra of a PEMFC contain comprehensive information on oxygen, proton and water transport inside the cell. However, extraction of transport parameters from the spectra requires sophisticated physics-based models [3–16] (see also reviews [17,18]).

In recent years, attempts have been made to calculate oxygen and proton transport resistivities by means of the distribution of relaxation times (DRT) technique [19–25]. DRT is based on formal expansion of EIS spectra over an infinite number of parallel *RC*-circuit impedances [23]. The resulting DRT spectrum consists of a number of peaks that represent the resonance *RC*-like impedances, which are attributed to separate transport and kinetic processes inside the cell. Unfortunately, the DRT peaks are not independent: variation of a single transport parameter in the PEMFC, *e.g.*, the CCL oxygen diffusivity D_{ox}, changes several peaks at once [26]. It has been shown analytically that the impedance of a two-layer oxygen transport system cannot be separated into a sum of two independent impedances [27]. More specifically, variation of oxygen diffusivity of one of the layers changes the impedances of both the layers. This impedes the correct attribution of peaks and makes it difficult to obtain the transport parameters by means of DRT spectra. A reliable method for measuring transport coefficients is the fitting of a physics-based impedance model to experimental spectra.

In some regimes, PEMFC spectra exhibit a low-frequency (LF) inductive loop. In spite of two decades of research, the origin of the loop

* Corresponding author.
E-mail addresses: tatyanar@hawaii.edu (T. Reshetenko), A.Kulikovsky@fz-juelich.de (A. Kulikovsky).

https://doi.org/10.1016/j.electacta.2024.145172
Received 4 April 2024; Received in revised form 18 July 2024; Accepted 28 September 2024
Available online 2 October 2024

Nomenclature

~	Marks dimensionless variables
b	ORR Tafel slope (V)
c	Oxygen molar concentration in the CCL (mol cm^{-3})
c_b	Oxygen molar concentration in the GDL (mol cm^{-3})
c_h	Oxygen molar concentration in the channel (mol cm^{-3})
c_v	Water vapor molar concentration (mol cm^{-3})
C_{dl}	Double layer capacitance (F cm^{-3})
D_b	Oxygen diffusivity of the GDL (cm^2 s^{-1})
D_{ox}	Oxygen diffusivity of the CCL (cm^2 s^{-1})
$D_{ox,d}$	Oxygen diffusivity of the dry CCL (cm^2 s^{-1})
D_v	Water vapor diffusivity in the CCL (cm^2 s^{-1})
e_0	Elementary charge (C)
F	Faraday constant (C mol^{-1})
h	Height of the channel (cm)
i	Imaginary unit
i_*	Volumetric ORR exchange current density (A cm^{-3})
J	Cell mean current density (A cm^{-2})
j	Local proton current density in the CCL (A cm^{-2})
K_l	CCL liquid water permeability (cm^2)
k_{pc}	Slope of capillary pressure and saturation (Pa)
k_σ	Coefficient in Eq. (8) (S cm^{-1})
k_l	Liquid transport coefficient (mol cm^{-1} Pa^{-1} s^{-1})
k_{lv}	Vaporization coefficient (mol cm^{-3} Pa^{-1} s^{-1})
l_t	CCL thickness (cm)
l_b	GDL thickness (cm)
p_v^s	Saturated vapor pressure at 80 °C at flat liquid–gas interface (bar)
p_c	Capillary pressure (Pa)
p_l	Liquid phase pressure (Pa)
p_g	Gas phase pressure (Pa)
p_{cell}	Overall cathode pressure (Pa)
Q_{ORR}	ORR rate (A cm^{-3})
Q_{lv}	Rate of evaporation/condensation (A cm^{-3})
r	Pore radius (cm)
R	Gas constant (J K^{-1} mol^{-1})
RH	Relative humidity ($0 \le$ RH ≤ 1)
s	CCL liquid saturation ($0 \le s \le 1$)
s_0	Reference liquid saturation ($0 \le s_0 \le 1$)
T	Cell temperature (K)
t	Time (s)
v	Air flow velocity in the channel (cm s^{-1})
V_l	Molar volume of liquid water (cm^3 mol^{-1})
x	Coordinate through the cell (cm)
z	Coordinate along the channel (cm)
Z	Electrochemical impedance (Ohm cm^2)

Subscripts

0	Membrane/CCL interface
1	CCL/GDL interface
b	GDL
h	Channel

Superscripts

0	Steady-state value
1	Small-amplitude perturbation

Greek

η	ORR overpotential, positive by convention (V)
λ	Air flow stoichiometry
μ_l	Viscosity of liquid water (Pa s)
κ	Vaporization rate constant (atm^{-1} cm^{-2}s^{-1})
ξ_{lv}	The evaporation interfacial area factor
σ	CCL proton conductivity (S cm^{-1})
σ_*	Reference CCL proton conductivity (S cm^{-1})
ω	Angular frequency of the AC signal (s^{-1})

remains controversial. Possible mechanisms include slow dynamics of ORR intermediates on the Pt surface [5,28], Pt surface oxidation [29,30], formation of hydrogen peroxide [29,31], water transport in membrane [10], relaxation of proton conductivity following liquid water transients in the CCL [16,32,33], and slow variation of air flow velocity during EIS measurements [34] (see also a review [35]).

Below, we extend our previous 1d + 1d physics-based model for PEMFC impedance by including liquid water transients in the CCL, following recent work [33]. Oxygen transport in the channel, gas diffusion layer, and CCL are taken into account as well. Liquid water transients induce slow variations of the CCL oxygen diffusivity and proton conductivity [33] which affect the low-frequency part of the spectra. The model is fitted to local experimental impedance spectra that have been measured for the segmented PEM fuel cell. The results reveal the minor variation of the CCL liquid water saturation and the growth of the "dry" CCL oxygen diffusivity with cell current density. Mechanisms behind these effects are discussed.

2. Experimental

Segmented cell setup (custom test station, a segmented hardware, current/voltage sensors and PXI data acquisition system) was constructed in Hawaii Natural Energy Institute (HNEI) and was used for measuring local impedance spectra. Detailed description of the segmented cell hardware is given in [36]. The pressure, humidity, gas flow rates, and total cell current or voltage were controlled by the test station. Local currents in individual segments were floating. Due to high electron conductivity of the cathode side elements, local segment potentials were assumed to be the same.

Fig. 1 shows a picture of the segmented cathode side of the cell. The hardware consists of a segmented flow field and current collector on one side, and non-segmented another side of the cell. The segmented flow field consists of ten segments with segment 1 at the inlet and segment 10 at the cell outlet. The same 10-channel parallel serpentine flow fields on either side of the cell were used in co-flow configuration

A commercially available catalyst coated membrane (CCM) with the active area of 100 cm^2 was used. The catalyst loading in both anode and cathode was 0.4 mg$_{Pt}$ cm^{-2}; the anode/cathode CCL thickness determined from SEM imaging varied in the range of 10–12 μm. The 16–18 μm reinforced Nafion 112 membrane and Sigracet 25BC gas diffusion layers (GDLs) on both sides of the cell were used. Optimal compression

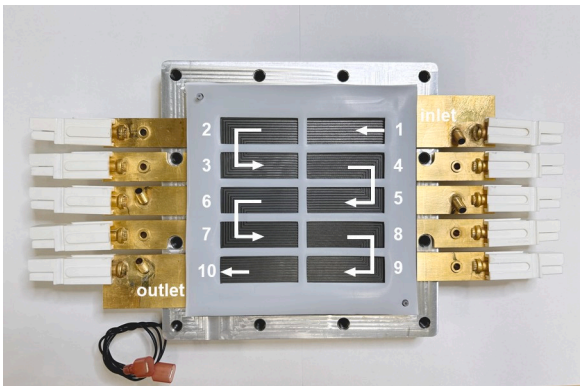

Fig. 1. Picture of the segmented cathode side of the cell. Arrows indicate direction of the air flow.

ratio of the MEA was achieved using Teflon gaskets of the thickness 125 μm for the anode and cathode. Due to the gasket and flow field segmentation, the active MEA area was reduced to 76 cm^2. The in-plane current between segments was estimated to be negligible compared to the through-plane current in the segments.

The cell temperature was fixed at 80 °C. The anode/cathode operating relative humidity and back pressure were 100/50% RH and 150/150 kPa, respectively. Hydrogen stoichiometry of 2 and air stoichiometry of 4 or 9.5 were used. The impedance spectra were measured under galvanostatic control of the overall cell in the frequency range from 10 kHz to 0.05 Hz with 11 steps/decade. The AC amplitude of current perturbation was set to get the voltage response amplitude of 10 mV. Co-flow configuration was used.

3. Model

3.1. Transport equations

Schematic of the PEM fuel cell cathode side with the straight channel and segmented electrodes, which modeled the experimental cell is shown in Fig. 2. The basic model assumptions are as following.

- The anode impedance is neglected.
- The electron conductivity of cell components is large.
- The cell is isothermal.
- Water transport in the GDL is ignored.
- The CCL liquid water permeability is independent of saturation.
- The total flux of water through the membrane is zero.

Water transport in the GDL will be incorporated in the next version of the model. Zero total flux of water in the membrane means that the electroosmotic flux of water from the anode side is compensated for by the back diffusion. This assumption will also be relaxed in the next model version.

The impedance model results from the transient mass- and charge-transport equations listed in Table 1. The system includes a plug-flow transport Eq. (1) for the oxygen concentration c_h in the channel, which is linked in a 1d + 1d manner to the through-plane diffusive transport Eq. (2) for the oxygen concentration c_b in the GDL.

The model of CCL performance in the single segment is based on standard macrohomogeneous transport equations with the oxygen diffusivity and proton conductivity dependent on liquid water content. The model of water transport in the CCL has been developed in [33].

For the sake of completeness, the complete model of CCL performance is briefly described below. A diffusion equation, Eq. (3), for the CCL oxygen concentration c is coupled to the proton charge conservation equation, Eq. (4), expressed in terms of the ORR overpotential η. Eq. (5) describes the evolution of the liquid saturation, s, related to the

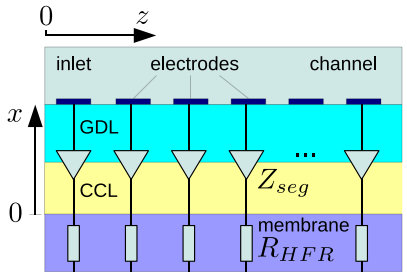

Fig. 2. Schematic of a PEMFC segmented cathode side with the straight channel.

Table 1
The governing equations for oxygen, water and proton transport. For the notations see Nomenclature section.

$\frac{\partial c_h}{\partial t} + v\frac{\partial c_h}{\partial z} = -\frac{D_b}{h}\left.\frac{\partial c_b}{\partial x}\right\|_{x=l_t+l_b}$	(1)	Channel
$\frac{\partial c_b}{\partial t} - D_b\frac{\partial^2 c_b}{\partial x^2} = 0$	(2)	GDL
$\frac{\partial c}{\partial t} - \frac{\partial}{\partial x}\left(D_{ox}\frac{\partial c}{\partial x}\right) = -\frac{Q_{ORR}}{4F}$	(3)	CCL
$C_{dl}\frac{\partial \eta}{\partial t} - \frac{\partial}{\partial x}\left(\sigma\frac{\partial \eta}{\partial x}\right) = -Q_{ORR}$	(4)	
$\frac{1}{V_l}\frac{\partial s}{\partial t} - \frac{K_l}{V_l\mu_l}\frac{\partial^2 p_l}{\partial x^2} = \frac{Q_{ORR}}{2F} - \frac{Q_{lv}}{2F}$	(5)	
$\frac{\partial c_v}{\partial t} - D_v\frac{\partial^2 c_v}{\partial x^2} = \frac{Q_{lv}}{2F}$	(6)	

liquid water pressure p_l, and Eq. (6) captures the diffusive transport of water vapor with concentration c_v in the CCL.

The rates of ORR, Q_{ORR}, and of liquid-to-vapor water conversion, Q_{lv}, are given by

$$Q_{ORR} = i_*\left(\frac{c}{c_h^0}\right)\exp\left(\frac{\eta}{b}\right),$$
$$Q_{lv} = \frac{2e_0\kappa\xi_{lv}}{l_t}\left(p_v^s - p_v\right), \tag{7}$$

where i_* is the volumetric ORR exchange current density, c_h^0 the reference (inlet) oxygen concentration, η the positive by convention ORR overpotential, b the ORR Tafel slope, e_0 the unsigned electron charge, κ the liquid water evaporation rate constant, ξ_{lv} the evaporation surface area factor, p_v^s the saturated water vapor pressure, and $p_v = c_v RT$ the water vapor pressure.

Parametric relations of the CCL oxygen diffusivity and proton conductivity with the liquid saturation, s, play an important role in this context. Following experiments [1], we assume that the proton conductivity, σ, in the CCL is proportional to s

$$\sigma = k_\sigma s. \tag{8}$$

For the oxygen diffusivity D_{ox}, we use the parametrization [37]

$$D_{ox} = D_{ox,d}(1-s)^2, \tag{9}$$

where $D_{ox,d}$ is the oxygen diffusivity of a dry CCL ("dry" diffusivity), corresponding to $s = 0$.

The liquid saturation is related to the capillary pressure through the water retention curve [38–40]. In this work, we have used the retention curve for low surface area carbon (LSAC) electrodes reported by Olbrich et al. [40]

$$s = s_0 + \frac{(1-s_0)}{2}\left(1 + \tanh\left(\frac{p_c - p_{c,0}}{k_{pc}}\right)\right) \tag{10}$$

(Fig. 3), where s_0 is pressure-independent residual saturation, $p_{c,0}$ determines position of the transition region where s varies from s_0 to unity, and k_{pc} describes the slope of the transition region. The numerical curve

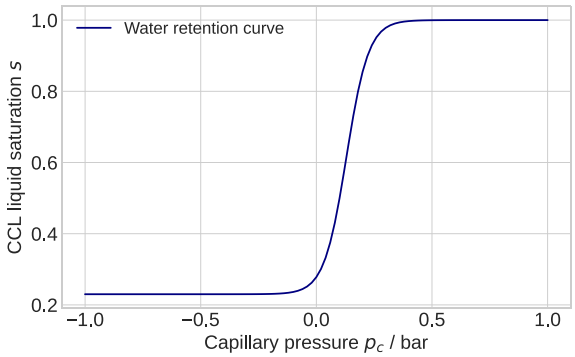

Fig. 3. The water retention curve of a low surface area carbon (LSAC) CCL from Olbrich et al. [40]. The curve parameters in Eq. (10) are: $s_0 = 0.23$, $p_{c,0} = 0.13$ bar, $k_{pc} = 0.096$ bar.

Table 2
The fixed cell parameters used in calculations.

Cathode relative humidity	RH	0.5	
Cathode pressure	p_{cell}	$1.5 \cdot 10^5$	Pa
Cell temperature	T	273 + 80	K
Saturated vapor pressure @ 80 °C	p_v^s	$0.446 \cdot 10^5$	Pa
Water vapor diffusivity	D_v	$2 \cdot D_{ox,d}$	
Exchange current density	i_*	$1 \cdot 10^{-3}$	A cm^{-3}
CCL thickness	l_t	$12 \cdot 10^{-4}$	cm
GDL thickness	l_b	$235 \cdot 10^{-4}$	cm
CCL liquid water permeability	K_l	$1 \cdot 10^{-14}$	cm^2
Molar volume of liquid water	V_l	18	cm^3 mol^{-1}
Viscosity of liquid water	μ_l	$8.9 \cdot 10^{-4}$	Pa s
Elementary charge	e_0	$1.6 \cdot 10^{-19}$	C
Evaporation rate constant	κ	$1.38 \cdot 10^{13}$	Pa^{-1} cm^{-2} s^{-1}
Evaporation surface area factor	ξ_{lv}	80	

parameters are indicated in caption to Fig. 3. The capillary pressure p_c (bar) is determined by

$$p_c = p_l - p_g, \tag{11}$$

with p_l, p_g being the liquid and gaseous pressures, respectively. More details on the CCL performance model can be found in [33].

3.2. Oxygen transport in the GDL and channel

Water transport in the GDL was ignored; two-phase water transport in the GDL will be incorporated in the next version of the model. In each segment, oxygen transport in the GDL is described by the diffusion equation Eq. (2). The boundary conditions for this equation are provided by solution to the plug-flow oxygen transport equation in the channel, Eq. (1) and by continuity of the oxygen flux at the GDL/CCL interface. On the other hand, solution of Eq. (1) requires the value of oxygen flux leaving the channel in every segment through the channel/GDL interface (the right side of Eq. (1)). Iterations are, therefore, unavoidable (see the next section).

3.3. Cell impedance and numerical procedures

Linearization and Fourier-transformation of equations in Table 1 leads to the system of linear complex-valued ODE for small perturbation amplitudes of the oxygen concentration c^1, c_b^1, c_h^1 and ORR overpotential η^1. In accordance with the experimental setup, the cell was separated into $N = 10$ segments along the cathode channel (Fig. 2). In every segment, the through-plane problem was solved using the oxygen concentration perturbation $c_h^1(z)$ in the channel as a boundary condition. Solution of the through-plane problem returns the perturbation of oxygen flux leaving the channel (the right side of Eq. (1)). With this parameter a new distribution of $c_h^1(z)$ is calculated; iterations are performed until convergence is achieved.

The segment impedance Z_{seg} is calculated as

$$Z_{seg} = -\left.\frac{\eta^1}{\sigma \partial \eta^1 / \partial x}\right|_{x=0} + i\omega L_{cab} S_{cell} + R_{HFR} \tag{12}$$

where L_{cab} is the cable inductance, S_{cell} is the cell active area, and R_{HFR} is the cell ohmic (high-frequency) resistance. The solution strategy is as follows. Impedance of the first segment can be calculated straightforwardly, taking zero inlet oxygen concentration perturbation as a boundary condition for the through-plane problem. The solution gives the flux $N_1 = D_b \partial c_b / \partial x|_{x=l_t+l_b}$ that leaves the channel to the first segment.

Eq. (1) for the second segment is solved using the flux N_1 from the first segment. Iterations between the "channel" and through-plane problems in the segment 2 solve this problem, which yields the oxygen flux $N_2 = D_b \partial c_b / \partial x|_{x=l_t+l_b}$ that leaves the channel to the second segment. In this way, the code "proceeds" from the inlet to the outlet.

The linear complex-valued system of equations was converted into real-valued equations for the real and imaginary parts of unknown functions. The resulting boundary-value problem (BVP) was solved using a standard Python BVP solver *solve_bvp*.

Seven parameters were declared as fitting ones: the ORR Tafel slope b, parameter k_σ in Eq. (8), the double layer capacitance C_{dl}, the "dry" oxygen diffusivity $D_{ox,d}$ in the CCL, the oxygen diffusivity D_b in the GDL, the ohmic resistance R_{HFR} of the cell, and the cable inductance L_{cab}. The constant parameters used in calculations are listed in Table 2. Fitting was performed using a nonlinear least-squares Python subroutine *least_squares* with the *method='trf'* key. The custom code for spectra fitting was parallelized using the MPI library by separating the whole frequency spectrum into 8 parts, according to the number of cores in the laptop CPU. Further details of the numerical procedure can be found in [41–43]. Fitting of 10 spectra corresponding to a fixed cell current density takes about 10 to 20 min on an 8-core notebook.

4. Results and discussion

4.1. Fitting of a spectrum from Gerling et al. [16]

Gerling et al. [16] published an experimental spectrum that is unique in literature, measured in the frequency range of 10 mHz to 100 kHz with 10 points per decade. The PEM fuel cell was operated at the current density of 1 A cm^{-2} and 30% humidity of the cathode flow (Figure S1 in [16]). Low RH of the cathode flow emphasizes the effects of liquid water transport in the CCL, making this spectrum an ideal dataset for testing the model.

Fig. 4 shows our model fitted to the spectrum [16]. In this calculation, two parameters of the water retention curve, $p_{c,0}$ and k_{pc} in Eq. (10), were declared as fitting ones. Fitting parameters are listed in the bottom part of Table 3. The high-frequency points above 20 kHz have been discarded, as in this frequency range the spectrum is determined mainly by the cable inductance. As can be seen, down to 100 mHz, our model fits the experiment [16] very well. The characteristic frequency of the inductive loop is about 200 mHz (the valley of $-\mathrm{Im}(Z)$, Fig. 4b). On the other hand, at 60 mHz the discrepancy between the model and experiment becomes noticeable and it rapidly increases with the degrease in frequency (Fig. 4b, left wing of the spectrum).

Two possible mechanisms of LF loop formation have been discussed in [16]: dynamics of Pt surface oxidation and slow relaxation of CCL proton conductivity. However, the model [16] is focused on Pt oxidation and it does not include liquid water transport in the CCL. The model spectra [16] indicate that the characteristic frequency of Pt surface oxidation/cleaning is about 10 mHz. Fig. 4b shows that the characteristic frequency of liquid water dynamics in the CCL is an order of magnitude higher, around 200 mHz.

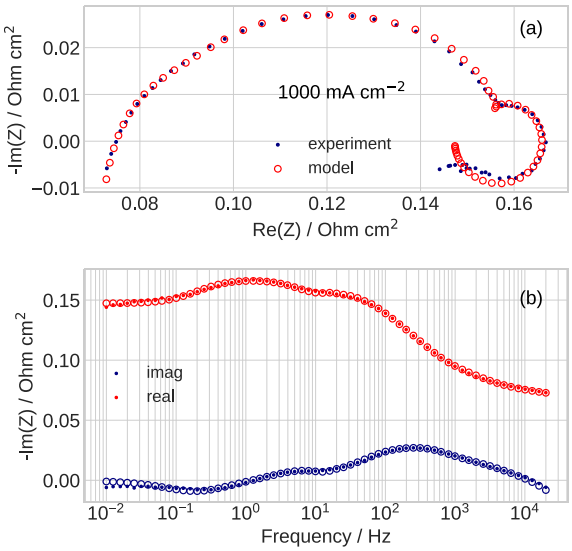

Fig. 4. (a) Experimental (points [16]) and fitted model (open circles) Nyquist spectra of the cell operated at the current density of 1 A cm^{-2}. The other operating parameters are listed in Table 3. The experimental points have been digitized from the spectra in Figure S1 [16]. (b) Real and imaginary part of the spectrum in (a) vs frequency.

Table 3
Top: the cell operating parameters reported by Gerling et al. [16]. Bottom: Fitted model parameters.

Cathode relative humidity	0.3
Cathode pressure, Pa	$1.5 \cdot 10^5$
Cell temperature, K	$273 + 80$
Current density, A cm^{-2}	1
Tafel slope, mV/dec	82 ± 3
CCL proton conductivity, mS cm^{-1}	13 ± 1
DL capacitance, F cm^{-3}	6.4 ± 0.4
CCL oxygen diffusivity, cm^2 s^{-1}	$(10 \pm 1) \cdot 10^{-4}$
GDL oxygen diffusivity, cm^2 s^{-1}	$(8 \pm 2) \cdot 10^{-2}$
$p_{c,0}$ in Eq. (10), bar	-0.04 ± 0.01
k_{pc} in Eq. (10), bar	0.09 ± 0.02
Mean CCL liquid saturation	0.26 ± 0.07

The inductive loop forms due to a slow relaxation of CCL liquid saturation s upon variation of gaseous and liquid pressures. The CCL proton conductivity is proportional to s, Eq. (8), and hence it follows the saturation. Due to the slow relaxation of s, the relaxation of current is delayed with respect to the perturbation of the cell potential, leading to an inductive-like response.

We presume that below 60 mHz, another LF mechanism not included in our model contributes to the spectrum, and this mechanism seemingly is Pt oxidation. Another reason for the discrepancy below 60 mHz could be the slow variations of the static cell parameters during impedance measurements. Anyway, assuming further that the characteristic frequency of Pt oxidation does not increase with the cell potential, we conclude that for current densities below 1 A cm^{-2}, our model works well down to $\simeq 60$ mHz.

4.2. Fitting our experimental spectra

Two sets of local spectra measured at the air flow stoichiometries of 4 and 9.5 in the frequency range of 50 mHz to 4 kHz were fitted. The spectra at $\lambda = 4$ where measured at the cell current densities of 50, 100, 200, 400, 600 and 800 mA cm^{-2} and at $\lambda = 9.5$ the spectra were acquired at 50, 100, 200, 300 and 400 mA cm^{-2}. Ten local spectra for every cell current density have been fitted, which amounts to 110 fitted spectra in total.

Fig. 5 shows examples of experimental and fitted model spectra from segment #6 of the cell operated at the current density of 400 mA cm^{-2} and air flow stoichiometry of 4. Note the low-frequency inductive "hook" caused by the slow relaxation of the CCL proton conductivity following the variation of electrode liquid saturation. Fig. 6 displays the local experimental and fitted Nyquist spectra for $J = 400$ mA cm^{-2} and the two stoichiometries. As can be seen, for all segments the quality of fitting is quite good through the whole frequency range.

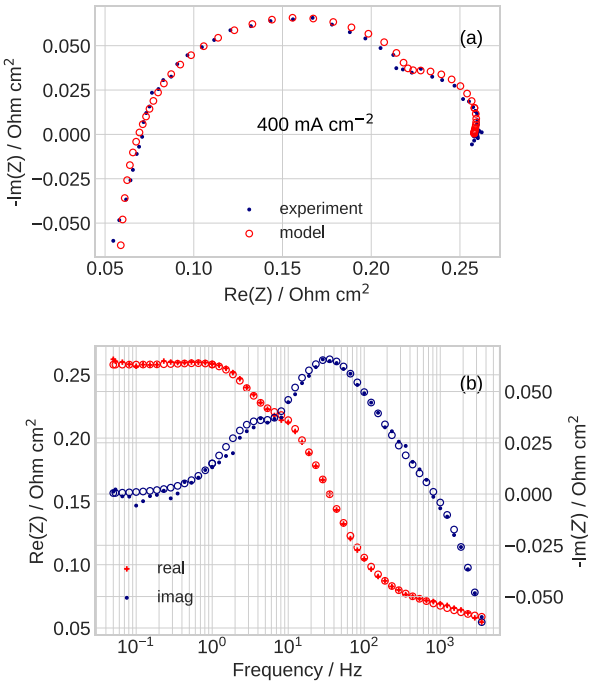

Fig. 5. (a) Experimental (points) and fitted model (open circles) Nyquist spectra of the segment #6 in the cell operated at the air flow stoichiometry of 4 and the current density of 0.4 A cm^{-2}. (b) Real and imaginary parts of the spectra in (a) vs. frequency.

Fig. 7 shows the shapes of local parameters through the CCL depth in segment #6 at the cell current density of 400 mA cm^{-2} and $\lambda = 4$. Liquid saturation decreases with distance from the membrane due to a strong liquid pressure gradient (Fig. 7a). Lowering of the liquid saturation toward the CCL/GDL interface induces a decay of the local proton conductivity and an increase in the oxygen diffusivity along x (Fig. 7b).

Fig. 8 shows the average CCL parameters resulting from spectra fitting as a function of cell current density. Each point in this figure is obtained by averaging of results over the ten segments. Whenever possible, the error bars were calculated using the covariance matrix obtained from the Jacobian returned by the fitting procedure. The variation of local parameters along the channel is not large and the mean values give a reliable picture of the dependence of cell transport parameters on current.

Contrary to common and intuitive belief, with the growth of cell current density J, the amount of liquid water in the CCL (mean liquid saturation) remains nearly constant: with J increasing from 50 to 800 mA cm^{-2}, the CCL liquid saturation increases by 20% (Fig. 8a). Nearly independence of J saturation is due to the growth of the liquid pressure gradient ∇p_l in the CCL, which facilitates removal of liquid water to the GDL (Fig. 7b). Fig. 8 demonstrates the strong coupling between s and ∇p_l: at currents above 400 mA cm^{-2}, the slope of ∇p_l growth lowers (Fig. 8b), leading to the faster growth of liquid saturation (Fig. 8a). In our model, liquid water transport through the GDL was ignored. Nonetheless, we may speculate that a high liquid pressure gradient in the CCL forming at high currents could possibly be the cause of GDL flooding. Indeed, due to much larger pore radii, the liquid pressure gradient in the GDL will be much smaller and water would tend to

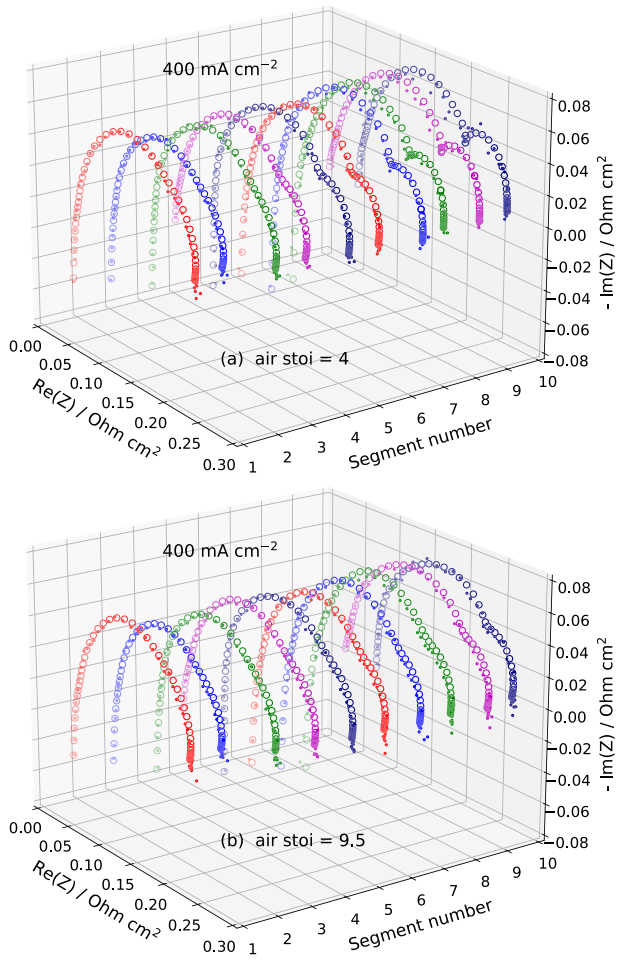

Fig. 6. (a) Experimental (points) and fitted model (open circles) local Nyquist spectra of the cell operated at the current density of 400 mA cm^{-2} and air flow stoichiometry of (a) 4 and (b) 9.5.

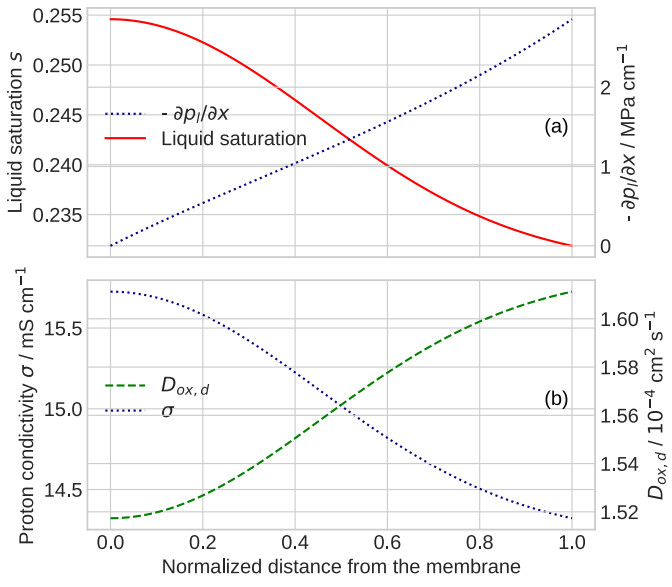

Fig. 7. The shapes of local parameters through the CCL depth resulting from fitting the spectrum from the segment #6, for $J = 400$ mA cm^{-2} and $\lambda = 4$. (a) Liquid saturation and liquid pressure gradient, (b) Proton conductivity σ and CCL "dry" oxygen diffusivity $D_{ox,d}$.

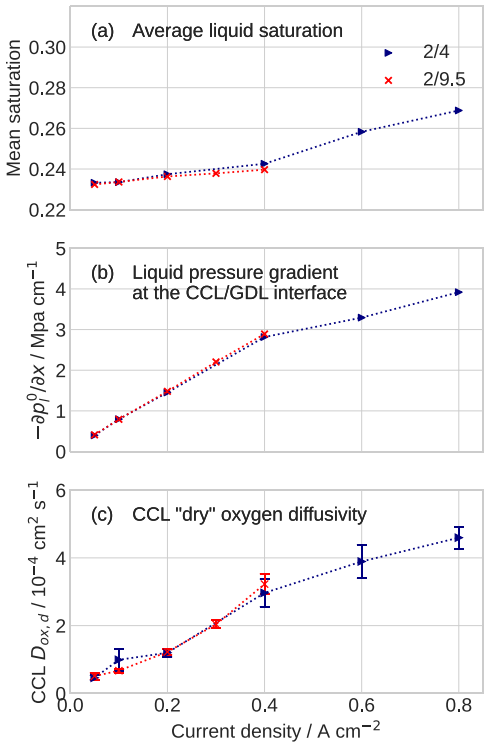

Fig. 8. The cell parameters resulted from spectra fitting vs cell current density for the hydrogen/air flow stoichiometries of 2/9.5 (red curves) and 2/4 (dark blue curves). Error bars are estimated from covariance matrix calculated using Jacobian returned by the fitting procedure.

accumulate in the GDL. In other words, at high currents, the CCL "pumps" liquid water to the GDL, where it could stagnate.

Of particular interest is Fig. 8c that demonstrates the growth of the dry CCL oxygen diffusivity $D_{ox,d}$, Eq. (9), with J. We attribute the effect to the following mechanism. Assuming that the pores have nearly circular cross section, it is easy to show that the total metal/electrolyte interfacial area would be much larger in small pores than it is in large pores [44]. Thus, at low current densities (50 and 100 mA cm^{-2}), most of the current is converted in small pores due to their large electrochemical surface area (ECSA). On the other hand, Knudsen diffusion coefficient in small pores is also small, meaning that the CCL effective oxygen diffusivity at small currents is low.

With the growth of cell current density, oxygen flux in small pores reaches limiting value and larger pores convert a growing part of the proton current. Since the oxygen diffusivity in larger pores is large, the apparent (effective) dry CCLoxygen diffusivity also increases. The process is illustrated schematically in Fig. 9 showing the pore size distribution (PSD) of a standard Gore CCL [45]. At small current density, proton current is converted in small pores (shaded area in Fig. 9). With the growth of J, the shaded area expands to the right, *i.e.*, larger pores get involved in the conversion. Since Knudsen diffusion coefficient is proportional to the pore radius, the effective CCL oxygen diffusivity measured by impedance spectroscopy increases with J.

The growth of the effective oxygen diffusivity with cell current has been detected in our previous works [41,42,46]. However, in [41,42,46] a simpler impedance model was used, which ignores the variation of the CCL effective oxygen diffusivity with liquid saturation. Fig. 8c leaves no doubt that the "dry" CCL oxygen diffusivity increases with J. The most probable mechanism is the expansion of the current-converting PSD fraction, as discussed above.

With the growth of J, the Tafel slope exhibits no distinct change (Fig. 10a). The absolute value of the Tafel slope agrees well with literature data for CCLs based on Pt/C catalyst [47]. The double layer

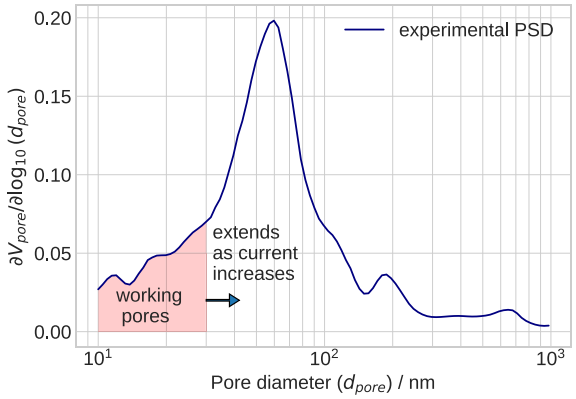

Fig. 9. Experimental pore size distribution in the CCL of a Gore electrode [45]. Shaded area depicts pores converting proton current at small cell current density J. With the growth of J, the shaded area expands to the right, meaning that larger pores with higher oxygen diffusivity convert growing part of the cell current.

capacitance decreases noticeably, while the CCL proton conductivity increases with the current as a result of growing proportionality coefficient k_σ in equation $\sigma = k_\sigma s$, Eq. (8) (Fig. 10b,c). The plot of k_σ vs J (not shown) reproduces the shape of the curve $\sigma(J)$ in Fig. 10c. The decrease in C_{dl} and the growth of k_σ could be caused by complete flooding of small pores with the growth of J. Both effects require further study. The high frequency resistance of the cell lies between 40 and 60 mOhm cm^2, which is a typical range of Nafion membranes. Higher R_{HFR} at $\lambda = 9.5$ is due to faster water removal from the cell cathode at higher air flow velocity.

5. Conclusions

Our physics-based 1d + 1d model for the impedance of a segmented PEM fuel cell is extended to take into account liquid water transport in the cathode catalyst layer [33]. Liquid water transients lead to variations of the CCL oxygen diffusivity and proton conductivity with the electrode water content. The model is fitted to the local experimental impedance spectra from PEMFC measured in the range of current densities from 50 to 800 mA cm^{-2}. The results demonstrate nearly constant with the cell current density mean liquid saturation in the CCL. The effect is due to the increase of liquid pressure gradient in the CCL facilitating liquid water removal. Another interesting feature is the linear growth of the "dry" CCL oxygen diffusivity $D_{ox,d}$, Eq. (9), with the cell current density. We attribute the growth of $D_{ox,d}$ to the following mechanism: At small currents, most of the current is converted in small pores due to their high cumulative active surface area. The Knudsen oxygen diffusivity of small pores is also small, which leads to small effective oxygen diffusivity of the electrode measured by EIS. With the growth of cell current, larger pores get increasingly involved in the current conversion, leading to increase in the apparent electrode oxygen diffusivity.

CRediT authorship contribution statement

Tatyana Reshetenko: Writing – original draft, Supervision, Methodology, Investigation, Data curation, Conceptualization. **Ying Sun:** Visualization, Validation, Software, Methodology, Investigation, Formal analysis. **Thomas Kadyk:** Project administration, Methodology, Investigation, Formal analysis, Conceptualization. **Michael Eikerling:** Writing – original draft, Supervision, Project administration, Methodology, Funding acquisition, Formal analysis, Conceptualization. **Andrei Kulikovsky:** Writing – original draft, Supervision, Software, Methodology, Investigation, Formal analysis, Conceptualization.

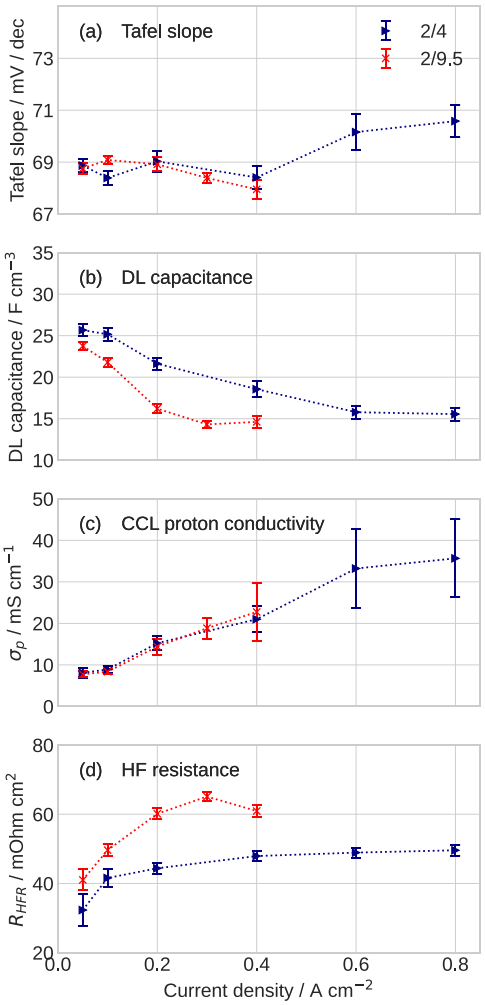

Fig. 10. The cell parameters resulted from spectra fitting vs. cell current density for the hydrogen/air flow stoichiometries of 2/9.5 (red curves) and 2/4 (dark blue curves). Error bars are estimated from the covariance matrix calculated using the Jacobian returned by the fitting procedure.

Declaration of competing interest

The authors declare that they have no known competing financial interests or personal relationships that could have appeared to influence the work reported in this paper.

Data availability

The data that has been used is confidential.

Acknowledgments

The authors acknowledge funding of the research presented in this article from the Helmholtz-Gemeinschaft Deutscher Forschungszentren e.V. (HGF), Program-oriented Funding (PoF IV), under the Research Program: Materials and Technologies for the Energy Transition (MTET). Tatyana Reshetenko gratefully acknowledges funding from the US Office of Naval Research (N00014-22-1-2045) and thanks G. Randolf and J. Huizingh for valuable help and support in system operation.

References

[1] T.E. Springer, T.A. Zawodzinski, S. Gottesfeld, Polymer electrolyte fuel cell model, J. Electrochem. Soc. 138 (8) (1991) 2334–2342.

[2] A. Lasia, Electrochemical Impedance Spectroscopy and Its Applications, Springer, New York, 2014.

[3] T.E. Springer, T.A. Zawodzinski, M.S. Wilson, S. Gottesfeld, Characterization of polymer electrolyte fuel cells using AC impedance spectroscopy, J. Electrochem. Soc. 143 (1996) 587–599, http://dx.doi.org/10.1149/1.1836485.

[4] M. Eikerling, A.A. Kornyshev, Electrochemical impedance of the cathode catalyst layer in polymer electrolyte fuel cells, J. Electroanal. Chem. 475 (1999) 107–123, http://dx.doi.org/10.1016/S0022-0728(99)00335-6.

[5] O. Antoine, Y. Bultel, R. Durand, Oxygen reduction reaction kinetics and mechanism on platinum nanoparticles inside nafion, J. Electroanal. Chem. 499 (2001) 85–94, http://dx.doi.org/10.1016/S0022-0728(00)00492-7.

[6] Y. Bultel, L. Genies, O. Antoine, P. Ozil, R. Durand, Modeling impedance diagrams of active layers in gas diffusion electrodes: Diffusion, ohmic drop effects and multistep reactions, J. Electroanal. Chem. 527 (2002) 143–155, http://dx.doi.org/10.1016/S0022-0728(02)00835-5.

[7] F. Jaouen, G. Lindbergh, Transient techniques for investigating mass–transport limitations in gas diffusion electrode, J. Electrochem. Soc. 150 (2003) A1699–A1710, http://dx.doi.org/10.1149/1.1624294.

[8] D. Gerteisen, A. Hakenjos, J.O. Schumacher, AC impedance modelling study on porous electrodes of proton exchange membrane fuel cells using an agglomerate model, J. Power Sources 173 (2007) 346–356, http://dx.doi.org/10.1016/j.jpowsour.2007.04.071.

[9] G. Maranzana, J. Mainka, O. Lottin, J. Dillet, A. Lamibrac, A. Thomas, S. Didierjean, A proton exchange membrane fuel cell impedance model taking into account convection along the air channel: On the bias between the low frequency limit of the impedance and the slope of the polarization curve, Electrochim. Acta 83 (2012) 13–27, http://dx.doi.org/10.1016/j.electacta.2012.07.065.

[10] C. Bao, W.G. Bessler, Two–dimensional modeling of a polymer electrolyte membrane fuel cell with long flow channel. Part II. physics–based electrochemical impedance analysis, J. Power Sources 278 (2015) 675–682, http://dx.doi.org/10.1016/j.jpowsour.2014.12.045.

[11] D. Gerteisen, Impact of inhomogeneous catalyst layer properties on impedance spectra of polymer electrolyte membrane fuel cells, J. Electrochem. Soc. 162 (2015) F1431–F1438, http://dx.doi.org/10.1149/2.0511514jes.

[12] A. Baricci, A. Casalegno, A simple analytical approach to simulate the electrochemical impedance response of flooded agglomerates in polymer fuel cells, Electrochim. Acta 157 (2015) 324–332, http://dx.doi.org/10.1016/j.electacta.2015.01.044.

[13] M. Obermaier, A.S. Bandarenka, C. Lohri-Tymozhynsky, A comprehensive physical impedance model of polymer electrolyte fuel cell cathodes in oxygen-free atmosphere, Sci. Rep. 8 (2018) 4933, http://dx.doi.org/10.1038/s41598-018-23071-5.

[14] A. Kosakian, M. Secanell, Estimating charge–transport properties of fuel–cell and electrolyzer catalyst layers via electrochemical impedance spectroscopy, Electrochim. Acta 367 (2021) 137521, http://dx.doi.org/10.1016/j.electacta.2020.137521.

[15] B. Najafi, P. Bonomi, A. Casalegno, F. Rinaldi, A. Baricci, Rapid fault diagnosis of PEM fuel cells through optimal electrochemical impedance spectroscopy tests, Energies 13 (2020) 3643, http://dx.doi.org/10.3390/en13143643.

[16] C. Gerling, M. Hanauer, U. Berner, K.A. Friedrich, Experimental and numerical investigation of the low-frequency inductive features in differential pemfcs: Ionomer humidification and platinum oxide effects, J. Electrochem. Soc. 170 (2023) 014504, http://dx.doi.org/10.1149/1945-7111/acb3ff.

[17] J. Huang, J. Zhang, Theory of impedance response of porous electrodes: Simplifications, inhomogeneities, non-stationarities and applications, J. Electrochem. Soc. 163 (2016) A1983–A2000, http://dx.doi.org/10.1149/2.0901609jes.

[18] Z. Tang, Q.-A. Huang, Y.-J. Wang, F. Zhang, W. Li, A. Li, L. Zhang, J. Zhang, Recent progress in the use of electrochemical impedance spectroscopy for the measurement, monitoring, diagnosis and optimization of proton exchange membrane fuel cell performance, J. Power Sources 468 (2020) 228361, http://dx.doi.org/10.1016/j.jpowsour.2020.228361.

[19] R. Fuoss, J. Kirkwood, Electrical properties of solids. VIII. Dipole moments in polyvinyl chloride-diphenyl systems, J. Am. Chem. Soc. 63 (1941) 385–394, http://dx.doi.org/10.1021/ja01847a013.

[20] H. Schichlein, A.C. Müller, M. Voigts, A. Krügel, E. Ivers-Tiffée, Deconvolution of electrochemical impedance spectra for the identification of electrode reaction mechanisms in solid oxide fuel cells, J. Appl. Electrochem. 32 (2002) 875–882, http://dx.doi.org/10.1023/A:1020599525160.

[21] M. Saccoccio, T.H. Wan, C. Chen, C. F, Optimal regularization in distribution of relaxation times applied to electrochemical impedance spectroscopy: Ridge and lasso regression methods - a theoretical and experimental study, Electrochim. Acta 147 (2014) 470–482, http://dx.doi.org/10.1016/j.electacta.2014.09.058.

[22] N. Bevilacqua, M. Schmid, R. Zeis, Understanding the role of the anode on the polarization losses in high-temperature polymer electrolyte membrane fuel cells using the distribution of relaxation times analysis, J. Power Sources 471 (2020) 228469, http://dx.doi.org/10.1016/j.jpowsour.2020.228469.

[23] B.A. Boukamp, Distribution (function) of relaxation times, successor to complex nonlinear least squares analysis of electrochemical impedance spectroscopy? J. Phys. Energy 2 (2020) 042001, http://dx.doi.org/10.1088/2515-7655/aba9e0.

[24] G.A. Cohen, D. Gelman, Y. Tsur, Development of a typical distribution function of relaxation times model for polymer electrolyte membrane fuel cells and quantifying the resistance to proton conduction within the catalyst layer, J. Phys. Chem. C 125 (2021) 11867–11874, http://dx.doi.org/10.1021/acs.jpcc.1c03667.

[25] Q. Wang, Z. Hu, L. Xu, Q. Gan, J Li, X. Du, M. Ouyang, A comparative study of equivalent circuit model and distribution of relaxation times for fuel cell impedance diagnosis, Int. J. Energy Res. 45 (2021) 15948–15961, http://dx.doi.org/10.1002/er.6825.

[26] A. Kulikovsky, A model–based analysis of PEM fuel cell distribution of relaxation times, Electrochim. Acta 429 (2022) 141046, http://dx.doi.org/10.1016/j.electacta.2022.141046.

[27] A. Kulikovsky, Analytical impedance of two–layer oxygen transport media in a PEM fuel cell, Electrochem. Comm. 135 (2022) 107187, http://dx.doi.org/10.1016/j.elecom.2021.107187.

[28] R. Makharia, M.F. Mathias, D.R. Baker, Measurement of catalyst layer electrolyte resistance in PEFCs using electrochemical impedance spectroscopy, J. Electrochem. Soc. 152 (2005) A970–A977, http://dx.doi.org/10.1149/1.1888367.

[29] S.K. Roy, M.E. Orazem, B. Tribollet, Interpretation of low-frequency inductive loops in PEM fuel cells, J. Electrochem. Soc. 154 (2007) B1378–B1388, http://dx.doi.org/10.1149/1.2789377.

[30] B.P. Setzler, T.F. Fuller, A physics–based impedance model of proton exchange membrane fuel cells exhibiting low–frequency inductive loops, J. Electrochem. Soc. 162 (2015) F519–F530, http://dx.doi.org/10.1149/2.0361506jes.

[31] S.K. Roy, M.E. Orazem, Deterministic impedance models for interpretation of low frequency inductive loops in PEM fuel cells, ECS Trans. 3 (2006) 1031–1040, http://dx.doi.org/10.1149/1.2356222.

[32] A. Kulikovsky, Effect of proton conductivity transients on PEM fuel cell impedance: Formation of a low–frequency inductive loop, Electrochem. Comm. 140 (2022) 107340, http://dx.doi.org/10.1016/j.elecom.2022.107340.

[33] Y. Sun, T. Kadyk, A. Kulikovsky, M. Eikerling, The effect of liquid saturation transients on PEM fuel cell impedance: Inductive loop and instability of catalyst layer operation, J. Electrochem. Soc. 171 (2024) 074506, http://dx.doi.org/10.1149/1945-7111/ad5efd.

[34] Q. Meyer, C. Zhao, Air perturbation-induced low-frequency inductive electrochemical impedance arc in proton exchange membrane fuel cells, J. Power Sources 488 (2021) 229245, http://dx.doi.org/10.1016/j.jpowsour.2020.229245.

[35] I. Pivac, F. Barbir, Inductive phenomena at low frequencies in impedance spectra of proton exchange membrane fuel cells – A review, J. Power Sources 326 (2016) 112–119, http://dx.doi.org/10.1016/j.jpowsour.2016.06.119.

[36] T.V. Reshetenko, G. Bender, K. Bethune, R. Rocheleau, Systematic study of back pressure and anode stoichiometry effects on spatial PEMFC performance distribution, Electrochim. Acta 56 (2011) 8700–8710, http://dx.doi.org/10.1016/j.electacta.2011.07.058.

[37] H. Fathi, A. Raoof, S.H. Mansouri, M.T. van Genuchten, Effects of porosity and water saturation on the effective diffusivity of a cathode catalyst layer, J. Electrochem. Soc. 164 (2017) F298–F305, http://dx.doi.org/10.1149/2.0871704jes.

[38] A. Kusoglu, A. Kwong, K.T. Clark, H.P. Gunterman, A.Z. Weber, Water uptake of fuel-cell catalyst layers, J. Electrochem. Soc. 159 (2012) F530, http://dx.doi.org/10.1149/2.031209jes.

[39] Y. Zhang, G. Agravante, T. Kadyk, M.H. Eikerling, Modeling water phenomena in the cathode side of polymer electrolyte fuel cells, Electrochim. Acta 452 (2023) 142228, http://dx.doi.org/10.1016/j.electacta.2023.142228.

[40] W. Olbrich, T. Kadyk, U. Sauter, M. Eikerling, Modeling of wetting phenomena in cathode catalyst layers for PEM fuel cells, Electrochim. Acta 431 (2022) 140850, http://dx.doi.org/10.1016/j.electacta.2022.140850.

[41] T. Reshetenko, A. Kulikovsky, Variation of PEM fuel cell physical parameters with current: Impedance spectroscopy study, J. Electrochem. Soc. 163 (9) (2016) F1100–F1106, http://dx.doi.org/10.1149/2.0981609jes.

[42] T. Reshetenko, A. Kulikovsky, Impedance spectroscopy characterization of oxygen transport in low– and high–pt loaded PEM fuel cells, J. Electrochem. Soc. 164 (2017) F1633–F1640, http://dx.doi.org/10.1149/2.1131714jes.

[43] T. Reshetenko, A. Kulikovsky, A model for extraction of spatially resolved data from impedance spectrum of a PEM fuel cell, J. Electrochem. Soc. 165 (2018) F291–F296, http://dx.doi.org/10.1149/2.0511805jes.

[44] T. Reshetenko, A. Kulikovsky, Oxygen transport in the low–Pt catalyst layer of a PEM fuel cell: Impedance spectroscopy study, Mat. Res. Express 10 (2023) 015501, http://dx.doi.org/10.1088/2053-1591/acaef3.

[45] H. Yu, L. Bonville, R. Maric, Analysis of H_2/Air polarization curves: The influence of low Pt loading and fabrication process, J. Electrochem. Soc. 165 (2018) F272–F284, http://dx.doi.org/10.1149/2.0261805jes.

[46] T. Reshetenko, A. Kulikovsky, PEM fuel cell characterization by means of the physical model for impedance spectra, J. Electrochem. Soc. 162 (2015) F627–F633, http://dx.doi.org/10.1149/2.1141506jes.

[47] H.A. Gasteiger, S.S. Kocha, B. Sompalli, F.T. Wagner, Activity benchmarks and requirements for Pt, Pt-alloy, and non-Pt oxygen reduction catalysts for PEMFCs, App. Catal. B: Env. 56 (2005) 9–35, http://dx.doi.org/10.1016/j.apcatb.2004.06.021.